Fully nonlinear features of the energetic beam-driven instability

Maxime Lesur, Y. Idomura, X. Garbet

HAL Id: hal-01722771

https://hal.science/hal-01722771

Submitted on 5 Mar 2018

Fully nonlinear features of the energetic beam-driven instability

M. Lesur,[1,2] Y. Idomura,[1] and X. Garbet[2]
[1]*Japan Atomic Energy Agency, Higashi-Ueno 6-9-3, Taitou, Tokyo 110-0015, Japan*
[2]*Commissariat à l'Energie Atomique, IRFM, F-13108 Saint Paul Lez Durance, France*

The so-called Berk–Breizman model is applied to a cold bulk, weak warm beam, one-dimensional plasma, to investigate the kinetic instability arising from the resonance of a single electrostatic wave with an energetic particle beam. A Vlasov code is developed to solve the initial value problem for the full-f distribution, and the nonlinear evolution is categorized in the whole parameter space as damped, steady-state, periodic, chaotic, or chirping. The saturation level of steady-state solutions and the bifurcation between steady-state and periodic solutions near marginal stability match analytic predictions. The limit of a perturbative numerical approach when the resonant region extends into the bulk is shown. Frequency sweeping is observed, with time-evolution approaching theoretical results. A new method to extract the dissipation rate from frequency diagnostics is proposed. For small collision rates, instabilities are observed in the linearly barely stable region. © *2009 American Institute of Physics.* [doi:10.1063/1.3234249]

I. INTRODUCTION

Containment of the energy of alpha particles is critical to achieve break even in magnetically confined fusion devices. In an ignited tokamak, these highly energetic particles can give birth to Alfvén wave instabilities in the form of isolated single modes. A concern is that these instabilities may lead to the premature ejection of the energetic population before they could give their energy to the core to sustain the reaction. In general, energetic particle driven instabilities are described in a three-dimensional (3D) configuration. However, near the resonant surface, it is possible to obtain a new set of variables in which the plasma is described by a one-dimensional (1D) Hamiltonian in two conjugated variables,[1–4] if we assume that a single resonance dominates. In this sense, there is a whole class of beam injection problems that are homothetic to a simple 1D single mode bump-on-tail instability. Observed quantitative similarities[1,5] between this class of beam instabilities and the so-called Berk–Breizman (BB) problem[3,4,6] are an indication of the validity of this reduction of dimensionality. This analogy enables more understanding of a fully nonlinear problem in a complex geometry by using a model that is analytically and numerically tractable, as a complementary approach to heavier 3D analysis. From these backgrounds, we investigate the kinetic features of the self-consistent interactions between an energetic particle beam and a weakly unstable electrostatic wave in 1D plasma.

The BB problem is an augmentation of the Vlasov–Maxwell system, where we take into account a collision term that represents particle annihilation and injection processes at a rate ν_a, and an external wave damping accounting for background dissipative mechanisms at a rate γ_d. In this system, we consider a bump-on-tail velocity distribution comprising a Maxwellian bulk and a beam of energetic particles, and we apply a small electrostatic perturbation. Depending on the parameters of the system, the perturbation may be damped or amplified due to the transfer of energy between resonant par-

ticles and the wave. In the unstable case, when the perturbation is small, the linear theory predicts exponential growth of the wave amplitude. Then the trapping of resonant particles significantly modify the distribution function and an island structure appears. The saturation of the instability and the following nonlinear evolutions are determined by a competition among the drive by resonant particles, the external damping, the particle relaxation which tends to recover the initial positive slope in the distribution function, and particle trapping that tends to smooth it. It has been predicted[3,4,6] and observed[7] that three kinds of behaviors emerge, namely, steady-state, periodic, or chaotic responses, depending on the strength of each factor. In addition, chaotic solutions can display shifting of the mode frequency (chirping), both upwardly and downwardly, as pairs of hole and clump are formed in the distribution.[8–10]

On the one hand, theories have been developed by Berk *et al.*[6,8–11] to predict the quantitative behavior of such instabilities in various parameter regimes and explain underlying mechanisms. The validity of some of these theories has been tested by numerical simulations based on a reduced model solving only resonant particles with adiabatic and cold bulk plasmas. A concern with this perturbative approach is that, as the instability grows, the resonant region may expand including a significant portion of bulk particles, and when chirping occurs, the resonant point may propagate into the bulk. In such situations, kinetic effects of the bulk plasma should also be taken into account. On the other hand, numerical simulations of the full distribution kinetics (full-f) have been performed by Vann *et al.*[7] in the whole (γ_d, ν_a) parameter space. However, in general, this approach shows some difficulty in simulating situations considered in the aforementioned theories, which assume a plasma near marginal stability with a cold bulk and a weak beam, and therefore, these theories have not been validated with this approach. To simulate such a situation, we need a robust and accurate numerical scheme.

The aim of this paper is to fill the gap between these two

fronts of the current state of research, with quantitative comparisons between available theory and nonreduced kinetic simulations. For this purpose, we develop a full-f Vlasov code based on the constrained interpolation profile-conservative semi-Lagrangian (CIP-CSL) scheme[12] for solving this initial value problem. We recall the equations of the BB model, present the main principles of our code, which will be referred to as BB-solver, and the equations of the reduced model in Sec. II. A first verification of the BB-solver consists of confirming its capability to solve the simpler Vlasov–Poisson system by recovering the saturation level, relative oscillation amplitude, and the so-called Bernstein–Greene–Kruskal (BGK) steady-state solution[13] in the collisionless limit without external damping. Then, we analyze the convergence and conservation properties of the BB-solver for a system with finite γ_d and ν_a, and benchmark it against a parameter scan given in former works by Vann.[7] Compared to this benchmark, our choice of parameters for testing the theory constitutes difficult conditions for numerical stability and drastically increases a computational cost. As a consequence, we must take special care in choosing an advection scheme that minimizes the computation time. Therefore a discussion of the relevancy of the CIP-CSL advection scheme and a comparison with four other advection schemes are provided in Sec. III. Armed with a verified set of numerical tools, we then proceed to the investigation of the validity of available theory. We apply the BB-solver to a distribution function comprising a cold bulk and a weak warm beam, and perform a systematic parameter scan in (γ_d, ν_a). The categorization of the nonlinear behavior of each solution is presented in the behavior bifurcation diagram of Sec. IV. In the whole parameter space, we observe a quantitative agreement between the numerical solution and analytic predictions for the linear growth rate. We validate the analytic theories for the following nonlinear features: saturation level in the parameter regime above marginal stability, saturation level and bifurcation criterion between steady-state and periodic solutions near marginal stability, and time-evolution of a frequency shifting mode. In this study, we compare our numerical results also with similar previous computations based on the reduced model, to show the limits of such model.

II. PHYSICAL AND NUMERICAL MODEL

A. The Berk–Breizman model

We cast the so-called BB model[14] as follows. We consider a 1D plasma with a distribution function $f(x,v,t)$. To ensure charge neutrality, we assume a background population of the opposite charge with a distribution function $\bar{f}(v,t)$, the space average of f. In the initial condition, the velocity distribution,

$$f_0(v) \equiv \bar{f}(v,t=0) = f_0^P(v) + f_0^B(v),\tag{1}$$

comprises a Maxwellian bulk,

$$f_0^P(v) = \frac{n_P}{v_P\sqrt{2\pi}}e^{-1/2(v/v_P)^2},\tag{2}$$

and a beam of high-energy particles,

$$f_0^B(v) = \frac{n_B}{v_B\sqrt{2\pi}}e^{-1/2(v-v_0/v_B)^2},\tag{3}$$

where n_P and n_B are bulk and beam densities, v_P and v_B are thermal velocities of bulk and beam particles, and v_0 is the beam drift velocity.

The evolution of the electronic distribution is given by the kinetic equation

$$\frac{\partial f}{\partial t} + v\frac{\partial f}{\partial x} + \frac{qE}{m}\frac{\partial f}{\partial v} = -\nu_a(v)(f - f_0),\tag{4}$$

where q is the charge, m is the mass, and E is the electric field. Here, collisions are taken into account in the form of a Krook operator[15] that is a model for both source and sink of energetic particles that tend to recover the initial distribution at a rate ν_a. If we assume cold and adiabatic bulk plasmas, $\nu_a(v)$ acts only on the beam. Reflecting this situation, we design the velocity dependency of $\nu_a(v)$ as

$$\nu_a(v) = \begin{cases} \nu_a & \text{if } v > v_\nu, \\ 0 & \text{else,} \end{cases}\tag{5}$$

with v_ν satisfying $f_P(v_\nu)/f_P(0)=\epsilon_\nu$, and we choose $\epsilon_\nu=0.001$. Hence, $\nu_a(v)$ is constant in the beam region and zero in the bulk region, except for the benchmark in Sec. III D where it is explicitly stated to be constant everywhere.

In the expression of the electric field,

$$E(x,t) = \hat{E}_k(t)e^{\imath kx} + \text{c.c.},\tag{6}$$

we assume a single mode of wave number k, reflecting the situation of a low toroidal mode number Alfvèn eigenmode, whose excited spectrum is usually discrete. The displacement current equation,

$$\frac{\partial E}{\partial t} = -4\pi q\int v(f - \bar{f})\mathrm{d}v - 2\gamma_d E,\tag{7}$$

yields the time evolution of the wave. The initial condition is given by solving Poisson's equation. In Eq. (7), an external wave damping has been added to model all linear dissipation mechanisms of the wave energy to the background plasma, which are not included in the previous equations. The factor 2 in front of γ_d has been chosen for the sake of simplicity and consistency with Berk and Breizman's literature. In the collisionless limit, if we assume a small perturbation and a linear growth rate γ much smaller than the real frequency ω, linear calculations yield the relation

$$\gamma = \gamma_L - \frac{2\gamma_d}{\dfrac{\omega}{\dfrac{\partial \mathcal{R}(D_L)}{\partial \Omega}\bigg|_{\Omega=\omega}}},\tag{8}$$

where γ_L is the linear growth rate in the absence of external damping, $\mathcal{R}(D_L)=1-4\pi q^2/m\Omega\mathcal{P}\int v\,\partial_v f_0/kv - \Omega dv$, and $\mathcal{P}$ is a notation for Cauchy's principal value. In the cold Maxwellian limit, a simple relation, $\gamma=\gamma_L-\gamma_d$, stands. However, with

our choice of distribution function, we must keep in mind that there is some discrepancy between γ and $\gamma_L - \gamma_d$.

In the ideal situation, the model presented above ensures conservation of the total particle number $N(t) \equiv \int f dx dv$. This is proven by taking the integral over the whole phase-space of the kinetic Eq. (4). We get

$$\frac{dN}{dt} = -\int \nu_a(v)(f - f_0) dx dv. \tag{9}$$

If $\nu_a(v) = \nu_a$ is taken as constant, the latter equation can be written as

$$\frac{d\Delta N}{dt} + \nu_a \Delta N = 0, \tag{10}$$

where $\Delta N(t) \equiv N(t) - N(0)$. Since $\Delta N(0) = 0$, Eq. (10) yields the total particle number conservation, $d\Delta N/dt = 0$. However, in numerical simulations, some spurious leakage of particles from the velocity boundaries induces a small error in this conservation. When $\nu_a(v)$ has the velocity dependence of Eq. (5), Eq. (10) is changed to

$$\frac{d\Delta N}{dt} + \nu_a \Delta N = \nu_a L \int_{-\infty}^{v_\nu} (\bar{f} - f_0) dv, \tag{11}$$

where $L = 2\pi/k$ is the system size. In the bulk part $v < v_\nu$, we assume that the variation of the distribution is negligible, $(\bar{f}(t) - f_0) \ll f_0$, and we show the approximative conservation of the total particle number,

$$\left| \frac{d\Delta N}{dt} + \nu_a \Delta N \right| \ll \nu_a N(0). \tag{12}$$

A straightforward analysis of the above model yields a power balance equation. Let us define the electric field energy density,

$$\mathcal{E}(t) \equiv \int \frac{E^2}{8\pi} \frac{dx}{L}. \tag{13}$$

The power transferred from the perturbed electric field to both bulk and beam particles, not including sloshing energy, is given by

$$P_h(t) \equiv q \int vEf dx dv. \tag{14}$$

We show the power balance equation,

$$P_E + P_h + P_d = 0, \tag{15}$$

where $P_E \equiv L d_t \mathcal{E}$ is the electric field power transfer, and $P_d \equiv 4L\gamma_d \mathcal{E}$ is the power transferred to the background plasma by dissipative mechanisms.

B. The BB-solver

The set of Eqs. (4)–(7), describing the fully nonlinear wave-particle interaction of the BB problem, is an extension of the Vlasov–Poisson system, which is recovered in the collisionless ($\nu_a = 0$) and closed system ($\gamma_d = 0$) limit. In a previous work,[16] we developed a 1D semi-Lagrangian Vlasov code, based on the cubic-interpolated-propagation (CIP)

scheme[17] and the splitting method,[18] which enabled accurate simulations of the Vlasov–Poisson system. In this work, we extend this code to include distribution relaxation and extrinsic dissipation.

Let us now describe the algorithm of our extended Vlasov solver or BB-solver. All quantities like f are sampled on uniform Eulerian grids with N_x and N_v grid points in the x and v directions, respectively, within the computational domain $\{(x, v) | 0 \le x < L, v_{min} \le v \le v_{max}\}$. The boundary conditions are periodic in the x-direction and fixed in the v-direction. We define the Courant–Friedrichs–Lewy number $CFL \equiv v_{max} \Delta t N_x / 2L$ as a measure of the time-step width Δt. We use the Strang splitting[19] formula to obtain a second-order accuracy in time.[7] For each time step, we perform the following steps.

(1) Advect $\partial_t f + v \partial_x f = 0$ for a time $\Delta t/2$.
(2) Solve $\partial_t f - \nu_a(v)(f - f_0) = 0$ for a time $\Delta t/2$.
(3) Solve $\partial_t E = -4\pi q \int v(f - \bar{f}) dv - 2\gamma_d E$ for a time $\Delta t/2$.
(4) Advect $\partial_t f + qE(x)/m \partial_v f = 0$ for a time Δt.
(5) Repeat the step 3.
(6) Repeat the step 2.
(7) Repeat the step 1.

Numerically, steps B and B are performed by a forward Euler scheme. The remaining problem, corresponding to steps 1 and 4, is the advection of a 1D hyperbolic equation,

$$\partial_t F + u \partial_\lambda F = 0, \tag{16}$$

where u is constant in the λ direction, λ is a generalized advection coordinate, and F is a general function of λ and t. In this work, we aim at long-time accurate simulations in the whole (γ_d, ν_a) space. The choice of advection scheme is of crucial importance to reach this goal. In Sec. III B, we show a comparison between different schemes, and from this comparison, we chose to use the CIP-CSL scheme. The key idea is that in addition to the distribution function, we advect its integrated value ρ to keep a flux balance between neighboring grids. In Appendix A, we recall the CIP-CSL algorithm for solving Eq. (16) and its extension to the position-velocity phase-space, as presented in Ref. 12.

C. Reduced model

In previous work,[20] the theory of the BB problem was investigated under a perturbative approach based on a particle code solving a reduced physical model.[21] The main hypothesis of this model is that the bulk particles interact adiabatically with the wave, so that their contribution to the Lagrangian can be expressed as a part of the electric field. This model describes only the time evolution of the beam part of the distribution f^B. Equations (4)–(7) are then replaced by

$$\frac{\partial f^B}{\partial t} + v \frac{\partial f^B}{\partial x} + \frac{q\tilde{E}}{m} \frac{\partial f^B}{\partial v} = -\nu_a(v)(f^B - f_0^B), \tag{17}$$

$$\widetilde{E}(x,t) \equiv \widetilde{E}_0(t)\sin(\xi + \phi) = \frac{mkS_k}{q}[Q\cos(\xi) - P\sin(\xi)], \quad (18)$$

where $\xi \equiv kx - \omega t$,

$$\frac{dQ}{dt} = n_B \int \frac{S_k}{k} f^B(x,v,t)\cos(\xi)\,dx\,dv, \quad (19)$$

$$\frac{dP}{dt} = n_B \int \frac{S_k}{k} f^B(x,v,t)\sin(\xi)\,dx\,dv, \quad (20)$$

where S_k is a normalization constant given by

$$S_k^2 \equiv \frac{\omega_0^3}{2\pi k n_0}, \quad (21)$$

where the plasma frequency is defined as $\omega_0^2 = 4\pi n_0 q^2/m$ and $n_0 \equiv \int f_0 dv = n_P + n_B$. To be able to compare our numerical results to previous work, we developed a reduced model Vlasov code based on the latter set of equations.

III. CODE VERIFICATION

Throughout this article, the wave number is fixed at $k = 0.3/\lambda_D$, where $\lambda_D = v_{th}/\omega_0$ is the Debye length, and v_{th} is the thermal velocity. The linear growth rate γ and the real frequency ω of the wave are defined as the exact solutions of the linear dispersion relation,

$$\gamma + 2\gamma_d - \iota\omega = \frac{\omega_0^2}{n_0}\int_\Gamma \frac{v\partial_v f_0}{(\gamma + \nu_a) + \iota(kv - \omega)}dv, \quad (22)$$

where Γ is the appropriate Landau contour.[22] The algorithm we implemented to solve the latter equation is based on a method of residue for locating the zeros of an analytic function in the complex plane.[23] In the following, γ_L is defined as the exact solution of the linear dispersion relation for $\gamma_d = \nu_a = 0$.

A. Collisionless closed system ($\gamma_d = \nu_a = 0$)

As a preliminary test, let us consider the simpler collisionless Vlasov–Poisson model without external damping, corresponding to the model of the BB problem (Sec. II A) without any particle source, sink, nor extrinsic dissipation. In the linear phase, the perturbation is much smaller than the unperturbed distribution, and the amplitude of the electric field follows an exponential growth of the bump-on-tail instability at a rate γ_L.[22] The linear growth goes on until the trajectories of resonant particles are significantly modified by electrostatic trapping. In the nonlinear phase, the distribution develops an island structure in phase space and becomes flat on average in the resonant velocity region. The instability saturates and the linear theory breaks down. Figure 1 shows the evolution of the normalized bounce frequency ω_b/γ_L, along with snapshots of the distribution function, for a cold bulk, weak warm beam initial distribution given in Sec. IV. Throughout this paper, the bounce frequency ω_b of particles that are deeply trapped in the electrostatic potential, defined as $\omega_b^2 \equiv |q|kE_0/m$, is used as a measure of the electric field amplitude E_0. We recover the linear growth rate obtained from our numerical eigenvalue solver with less than 1% er-

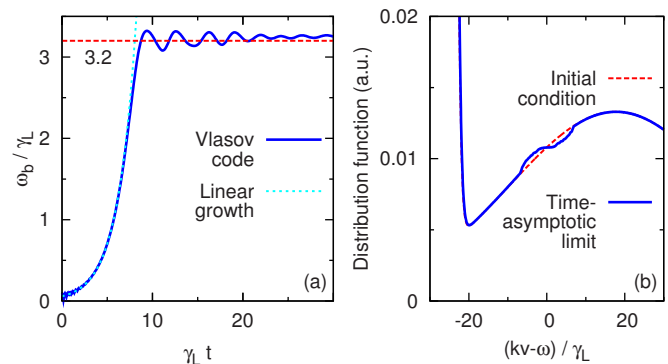

FIG. 1. (Color online) Nonlinear evolution of the normalized bounce frequency (a) and snapshots of the distribution function, normalized to n_0/v_{th} (b), for $\gamma_d = \nu_a = 0$, the initial distribution given in Sec. IV, and $N_x \times N_v = 256 \times 2048$ grid points.

ror. The saturation level is close to the value $\omega_b/\gamma_L \sim 3.2$, which was numerically obtained in Ref. 24 via a particle code with the above mentioned adiabatic cold bulk reduced model.

In the time-asymptotic limit, the steady-state solution of the Vlasov–Maxwell system is a distribution given as a function only of the energy. The BGK solution is consistent with a nonzero electric field. Figure 2 is a contour plot of the distribution function in the time-asymptotic limit of the numerical simulation, on which several constant energy curves are superposed. We clearly observe the island structure, which agrees with the BGK solution.

B. Convergence properties

In choosing an advection scheme, we focus on the stability and convergence properties, which are estimated in severe benchmark parameters relevant for analyses in Sec. IV, where we use a distribution with a cold bulk and a weak warm beam. Compared to the simulation parameters applied in the following benchmark (Sec. III D), this simulation con-
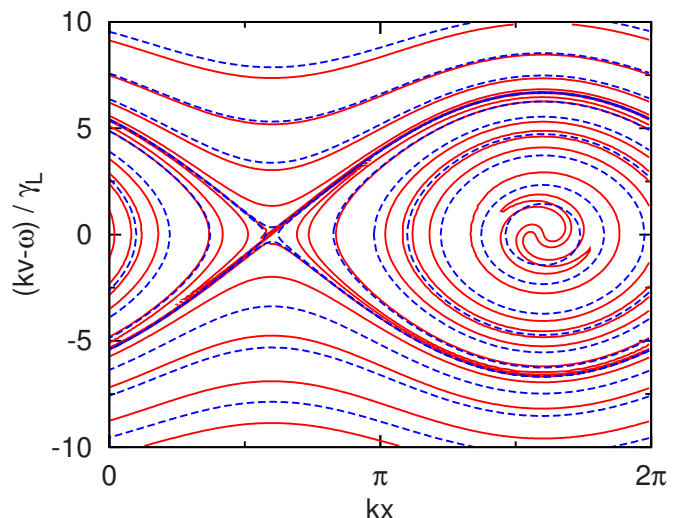

FIG. 2. (Color online) Contour plot of the time-asymptotic distribution function (solid curves) and constant energy curves (dashed curves) for the same parameters as Fig. 1.
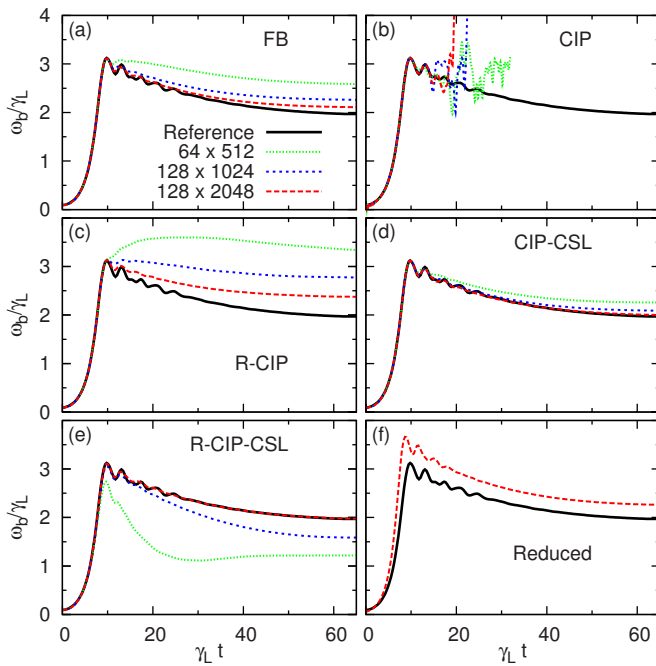
FIG. 3. (Color online) Time evolution of the normalized bounce frequency for five advection schemes (a)–(e), and with the reduced model (f). Solutions are shown for grid resolution $N_x \times N_v$ of 64×512, 128×1024, and 128×2048, and for a reference run described in the text. The initial distribution is given in Sec. IV. The other parameters of these simulations are $\nu_a(v > v_\nu) = 0.002\omega_0$, $\gamma_d = 0.002\omega_0$, CFL$=0.9$, $v_{\min} = -10v_{\text{th}}$, and $v_{\max} = 18v_{\text{th}}$.

FIG. 4. (Color online) Time evolution of the power balance. P_E, P_d, and P_h are the electric field, dissipative, and particle power transfers, respectively. The solid curve is the sum of these three power transfers. The parameters of the simulations are similar to Fig. 3, for 64×512 grids.

dition is more sensitive to numerical errors such as numerical diffusion. First, the colder the bulk, the less grids become available in the bulk, leading to artificial heating. Second, the weak warm beam induces weaker linear instabilities, which produce narrower islands in phase space. To resolve such a narrow island, increased grid resolution is needed. Furthermore, for steady-state solutions, when the island is narrower we observe unphysical drive after nonlinear saturation, which suggests that the region of flattening acquires spurious gradient by influence of the surrounding distribution. In this work, we aim at producing a numerical scan of the nonlinear behavior in the whole parameter space. Near marginal stability, the linear growth rate γ is very small (we limit the investigation range to $|\gamma| > 10^{-6}\omega_0$ to avoid excessive computation cost) and long-time computations ($\omega_0 t \sim 10^5$) are required. For this reason, we cannot afford too much grid points, and we have to take utmost care in choosing a robust and quickly converging numerical scheme.

A comparison of several advection schemes for one of the cases of Fig. 6 (cold bulk, weak warm beam, and $\gamma_L/\omega_0 = 0.0324$) is shown in Fig. 3. The time evolution of a beam instability with a low dissipation $\nu_a(v > v_\nu) = 0.002\omega_0$ and a small external damping $\gamma_d = 0.002\omega_0$, for increasing grid resolution, is compared to a reference run for each of five schemes: flux-balance (FB),[25] CIP,[17] CIP with rational function interpolation (R-CIP),[26] CIP-CSL, and rational-CIP-CSL (R-CIP-CSL) schemes.[27] The reference run is obtained with a high resolution $N_x \times N_v = 256 \times 4096$ using CIP-CSL. The CIP scheme is a low-diffusion and stable scheme and is implemented in a way that exactly conserves the total mass. However, it is not locally conservative. After several ampli-
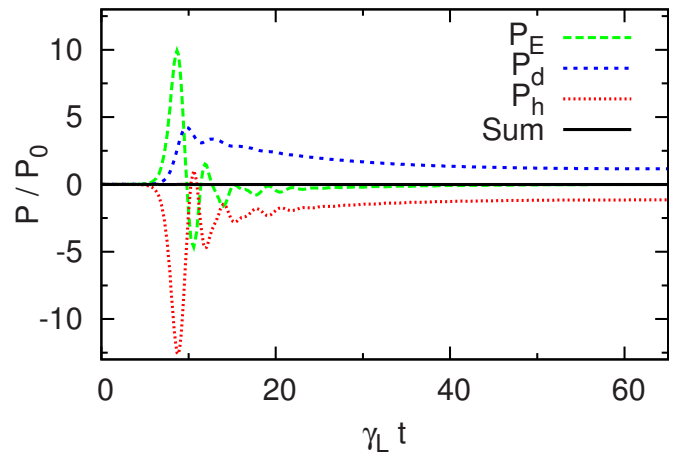
tude oscillations in the nonlinear phase, we observe the apparition of numerical oscillations in the velocity direction in a large gradient region of the distribution, which appears between a cold bulk and a beam. While, in this test case, numerical divergence eventually occurs even for very high resolution with the CIP scheme, the other schemes show convergence to the same solution. The FB scheme is only second order accurate, so that the convergence is slow compared to the CIP-based schemes, which have a third order accuracy in general.[17] Rational function interpolation aims at preventing numerical oscillation by preserving convex-concave and monotonic properties, but at the expense of this property, its numerical diffusion produces spurious drive leading to higher saturation levels. R-CIP-CSL produces less numerical diffusion than R-CIP, but the convergence is relatively slow for both. Finally, the CIP-CSL scheme shows quick convergence without unfavorable numerical oscillations, and therefore, we use this scheme in the following simulations.

As an illustration of the reduced model Vlasov code, we include, in Fig. 3, the time evolution of the beam instability obtained by the reduced model (with the CIP-CSL scheme), for the same parameters as those of the nonreduced simulations.

C. Conservation properties

The total particle number in the simulations is calculated by taking the sum over the computation domain of the integrated value of the electronic distribution, $N(t_n) = \Sigma_{i,j}\rho_{i,j}^n$. When ν_a is a constant, the relative error in particle conservation is of the order of the machine precision ($<10^{-12}\%$), as is expected from a conservative scheme. Even when $\nu_a(v)$ has the velocity dependence of Eq. (5), the relative error is negligible ($<10^{-9}\%$). In both cases, numerical simulations show a good fidelity to the power balance, even for a relatively small number of grid points. Figure 4 shows how the different power transfers (normalized to

$P_0 \equiv m L n_0 v_{th}^2 \omega_0 (\gamma_L/\omega_0)^4/2)$ compensate with each other. The order of the relative error in power balance, $|P_E + P_d + P_h|/(|P_E| + |P_d| + |P_h|)$, is 0.1%.

D. Benchmarking: Bifurcation diagram in the (γ_d, ν_a) space

We consider five kinds of behaviors for the time evolution of the instability. The category is obtained by an analysis of the electric field energy density $\mathcal{E}(t)$ and the frequency spectrum. A numerical solution is defined as

(1) damped: if the asymptotic-time limit of $\mathcal{E}(t)$ is zero;
(2) steady-state: if the asymptotic-time limit of $\mathcal{E}(t)$ is finite;
(3) periodic: if for large enough t there is a period τ for which $\mathcal{E}(t+\tau) \to \mathcal{E}(t)$;
(4) chirping: if there is a spectral component whose frequency significantly shifts in time;
(5) chaotic: if $\mathcal{E}(t)$ is bounded, but does not satisfy one of the previous conditions.

The categories (1), (2), (3), and (5) are defined in the same way as Vann,[7] and we added a new diagnosis for the characterization of chirping solutions. Each numerical solution is systematically categorized by an algorithm based on a decision tree, which is based on the one developed by Vann. We describe this algorithm in Appendix B.

As a benchmark of both the BB-solver and the categorization algorithm, we reproduce the results presented in Fig. 3 of Ref. 7 (Note that our definition of γ_d is consistent with Berk and Breizman's literature and differs from Vann's article by a factor of 2.) The initial distribution is given by $n_B/n_0 = 0.1$, $v_P = v_{th}$, $v_B = 0.5 v_{th}$, $v_0 = 4.5 v_{th}$, so that $\gamma_L/\omega_0 = 0.1981$. The field energy of the initial perturbation is 2×10^{-4} of the total energy, which corresponds to $\omega_b/\gamma_L = 0.05$ at $t=0$. We perform a series of simulations in the parameter space (γ_d, ν_a), where ν_a is chosen as velocity independent. We set the time duration of each simulation to $\omega_0 t_{max} = 3000$. In the categorization algorithm, we choose $\omega_0 t_{min} = 1000$, $\epsilon_1 = 10^{-12}$, $\epsilon_2 = 0.05$, $\epsilon_3 = 0.01$, $\epsilon_4 = 10^{-9}$, and $\epsilon_5 = 0.25$. The resulting behavior bifurcation diagram is shown in Fig. 5. The 1416 simulations used for this plot took approximately 115 CPU h on an Altix3700Bx2 array of Intel Itanium2 processors. The categorization of 92% of these time series is in agreement with the reference, most of the difference coming from a different way of sorting out chaotic from periodic solutions. This result is a further indication of the validity of both the BB-solver and categorization algorithm.

IV. APPLICATION TO AVAILABLE THEORY

In this section, we apply the above numerical algorithms to investigate the validity of the BB theory in several regions of the (γ_d, ν_a) parameter space. The initial bump-on-tail distribution parameters are chosen such that we stay within the validity limit of the theory, with a cold bulk and a weak warm beam as $n_B/n_0 = 0.1$, $v_P = 0.2 v_{th}$, $v_B = 3 v_{th}$, and $v_0 = 5 v_{th}$, which give $\gamma_L/\omega_0 = 0.0324$, $\omega/\omega_0 = 0.925$. We recall that ν_a is a function of the velocity such that collisions affect only the beam particles. The field energy of the initial per-
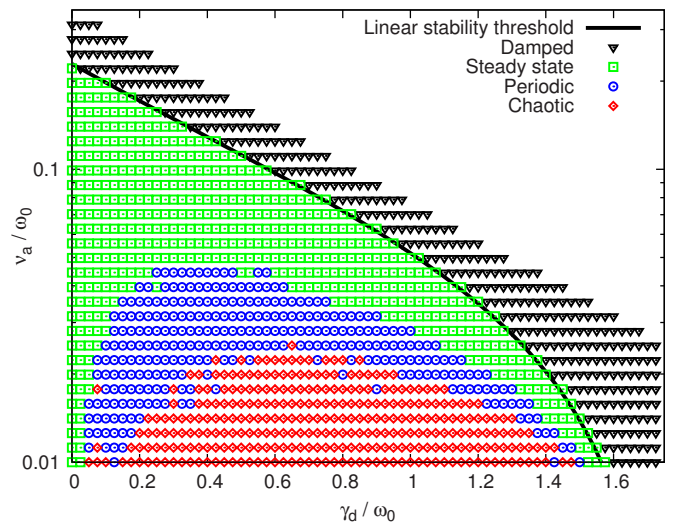

FIG. 5. (Color online) Behavior bifurcation diagram. The classification of each solution is plotted in the (γ_d, ν_a) parameter space. The solid curve is the linear stability threshold obtained by solving the linear dispersion relation numerically. The parameters of these simulations are $N_x \times N_v = 64 \times 512$, CFL=1.2, and $v_{max} = -v_{min} = 8 v_{th}$.

turbation is 2×10^{-8} of the total energy or $\omega_b/\gamma_L = 0.3$. For the benchmark, we set the same value for the maximum time of every numerical simulation. However, we now take into account the increase in computational cost when the chosen initial distribution gives such a small γ_L. As we approach the marginal stability, the time window must be increasingly large to successfully capture the behavior of the solution. To reduce the computational cost, we choose the time window size as a function of γ, as

$$t_{max} = 20 \frac{2\pi}{|\gamma|}. \tag{23}$$

The frequency of amplitude oscillations is of the order of ω_b, which is empirically of the order of γ after the transient phase, so that such time windows contain at least a few amplitude oscillations, enough to sort steady state, periodic, and chaotic responses. In the categorization algorithm, we choose $t_{min} = t_{max}/2$ and each time series is sampled every $\Delta t_s = 20/\omega_0$. $\epsilon_0 = 10^{-14}$ is chosen as a free-streaming criterion, $\epsilon_6 = 0.05$, $\epsilon_7 = 0.05$ are used to sort out chirping solutions, and the other ϵ-thresholds are the same as above. The characterization of the behavior of the wave amplitude obtained by the BB-solver is shown in Fig. 6. The 391 simulations used for this plot required approximately 15 000 CPU h on an Altix3700Bx2 array of Intel Itanium2 processors.

The agreement between the linear stability threshold and the boundary between linearly stable and unstable simulations confirms that the problem of recurrence is taken care of by the free streaming test in the categorization algorithm. When $\gamma_d \ll \gamma_L$ and $\nu_a \ll \gamma_d$, a bursty behavior, characterized by a succession of bursts with characteristic growth and decay rates of γ_L and γ_d, respectively, and with a quiescent phase in between that lasts a time $1/\nu_a$, as described in Ref. 28, is expected. A few solutions in the chaotic region appear to follow this picture. However, most of the chaotic solutions do not feature a significantly quiescent phase. Consequently,
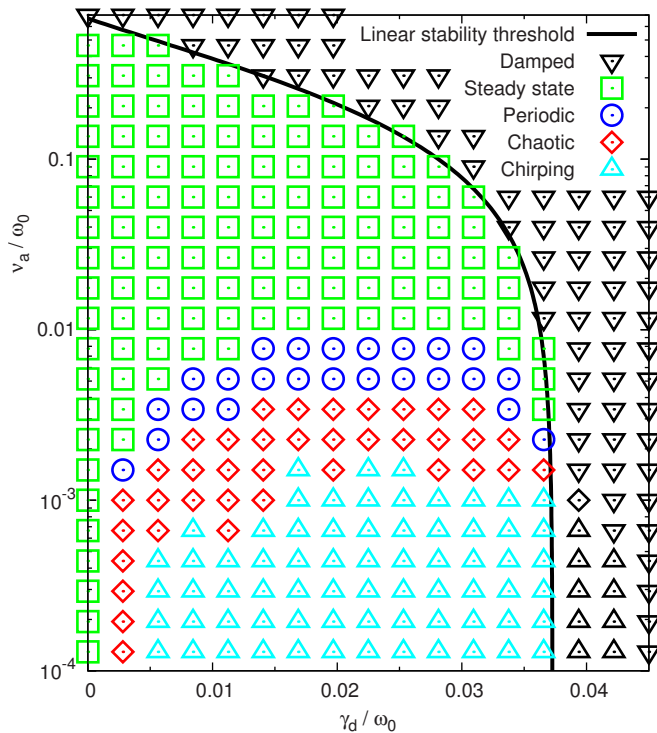
FIG. 6. (Color online) Behavior bifurcation diagram for a cold bulk, weak warm beam distribution for which $\gamma_L/\omega_0 = 0.0324$. The classification of each solution is plotted in the (γ_d, ν_a) parameter space. The solid curve is the linear stability threshold obtained by solving the linear dispersion relation numerically. The parameters of these simulations are CFL=3.0, $v_{max} = 18v_{th}$, $v_{min} = -10v_{th}$, $N_v = 2048$, and N_x ranges from 128 to 256. Diamonds and triangles on the right of the linear stability threshold, which are not included in the legend, represent subcritical instabilities.

an attempt at sorting out a pulsating regime from the chaotic region seems vain. For small collision rates, we observe instabilities in the linearly stable region, which suggests the possibility of subcritical instabilities. This effect is not discussed in this article but will be the subject of future work. The physics of several region of this diagram is discussed in the following subsections.

A. Steady state above marginal stability ($\gamma_d \sim \nu_a \ll \gamma_L$)

In the parameter region where external damping and distribution relaxation are of the same order and both are small compared to the linear drive, we expect and observe the saturation of the wave amplitude to a steady state in the time-asymptotic limit. We assume a rate of annihilation of the beam particles much smaller than the saturated bounce frequency, $\nu_a \ll \omega_b$ at $t \to \infty$. We also assume that the resonant region is narrow compared to the resonant velocity, $4\omega_b/k \ll \omega/k$, so that we can assume that the contribution to the resonant power transfer comes from a narrow region around the resonant velocity. Berk and Breizman derived a relation yielding the saturation level in this situation,[11]

$$\omega_b = 1.96 \frac{\nu_a}{\gamma_d} \gamma_L. \tag{24}$$

Thus, if we normalize all quantities to the linear growth rate, then within the aforementioned assumptions, the saturation level depends only on the ratio of ν_a to γ_d.
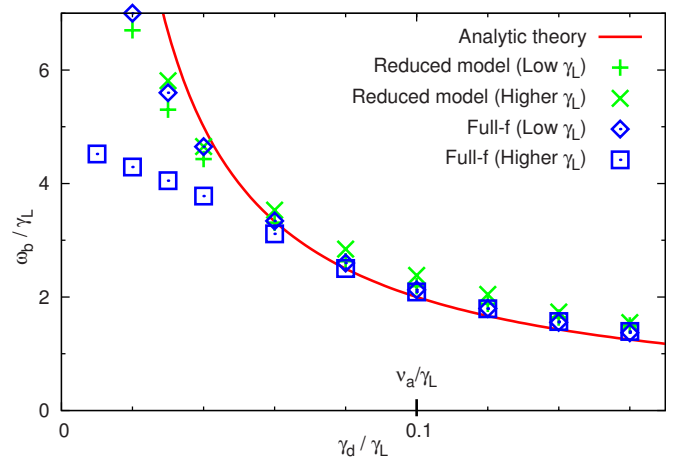

FIG. 7. (Color online) Saturation level at a given collision frequency $\nu_a/\gamma_L = 0.1$ for both the distribution of Fig. 6 (Low-γ_L case), and a distribution with increased beam density (Higher-γ_L case). The numerical parameters of the simulations are those of Fig. 6.

We investigate the validity of this theory by numerically computing the scaling law for the saturation level at a given normalized relaxation rate $\nu_a/\gamma_L = 0.1$. In a previous work,[20] such a scan has been done using a reduced model particle code, and the results showed good agreement with the analytic prediction in a region where $\gamma_d \sim \nu_a$. Figure 7 shows the saturation level obtained from the analytical theory, Eq. (24), from reduced model simulations, and from full-f simulations with the BB-solver. When the initial distribution is the one used in Fig. 6, we observe quantitative agreement between the theory and both reduced model and full-f simulations in the parameter region $\gamma_d \sim \nu_a$.

To reveal the limitations of the reduced model, the same computation is done for a distribution with a slightly increased beam density ($n_B/n_0 = 0.15$) and decreased beam temperature ($v_B/v_{th} = 2.5$), giving $\gamma_L/\omega_0 = 0.067$ instead of 0.032. When we use the reduced model, the scaling law is roughly independent of γ_L and is in agreement with the theory in the parameter region $\gamma_d \sim \nu_a$, in accordance with the aforementioned work. On the other hand, when we take into account the evolution of bulk plasma, we observe a significant dependency of the saturation amplitude on the linear growth rate. For larger γ_L, we find some discrepancy from the analytical prediction in the low γ_d region because the island width becomes of the order of the resonant velocity (The island width normalized to the resonant velocity is given by $0.14\omega_b/\gamma_L$ in the low-γ_L case and by $0.29\omega_b/\gamma_L$ in the higher-γ_L case.) This result shows that it is necessary to take into account the effect of bulk particles to accurately discuss the validity limit of the theory.

B. Steady state and periodic solutions near marginal stability ($\gamma \approx \gamma_L - \gamma_d \ll \gamma_L$)

When $\gamma \ll \gamma_L$, a reduced integral equation for the time evolution of the electric field amplitude has been developed using an extension based on the closeness to marginal stability.[6] Within the assumption $\omega_b/\gamma \ll 1$,
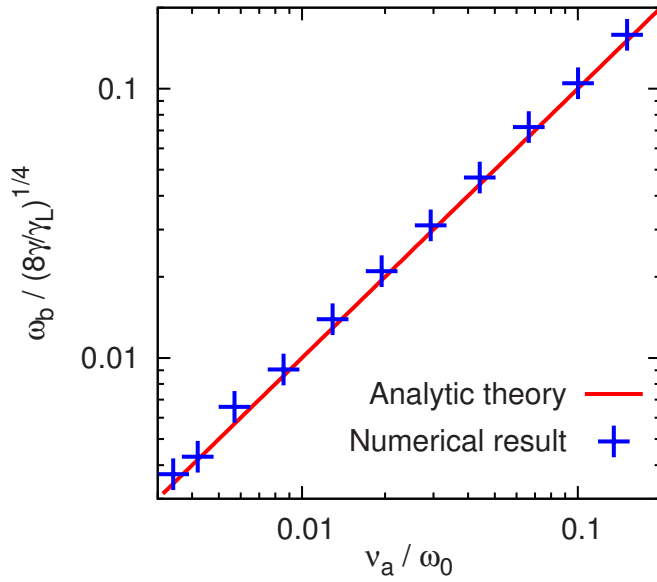
FIG. 8. (Color online) Saturation level of solutions near marginal stability for the distribution and the numerical parameters of Fig. 6.
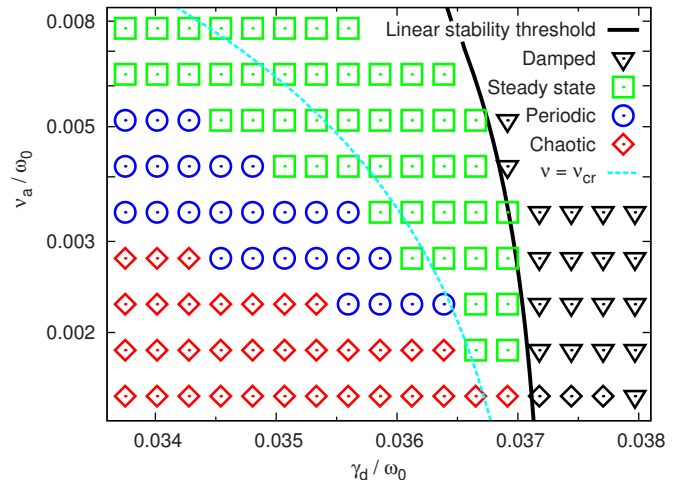

FIG. 9. (Color online) Zoom in the behavior bifurcation diagram (Fig. 6) of the region near marginal stability where the steady state periodic bifurcation occurs, along with the critical distribution relaxation. Diamonds on the right of the linear stability threshold, which are not included in the legend, correspond to subcritical instabilities.

$$\frac{d\omega_b^2}{dt} = (\gamma_L^* - \gamma_d)\omega_b^2 - \frac{\gamma_L^*}{2}\int_{t/2}^{t}dt_1\int_{t-t_1}^{t_1}dt_2(t-t_1)^2$$
$$\times e^{-\nu_a(2t-t_1-t_2)}\omega_b^2(t_1)\omega_b^2(t_2)\omega_b^2(t+t_2-t_1), \quad (25)$$

where γ_L^* is the linear growth rate obtained by solving analytically the dispersion relation for $\gamma_d = \nu_a = 0$ in the γ, $\sqrt{2}k v_{\text{th}} \ll \omega$ limit,

$$\gamma_L^* \equiv \frac{\pi}{2n_0}\frac{\omega_0^2\omega}{k^2}\left.\frac{\partial f_0}{\partial v}\right|_{v=\omega/k}. \quad (26)$$

For a cold bulk, warm beam distribution, an analytic treatment of the dispersion relation (22) yields

$$\gamma \approx \gamma_L^* - \gamma_d, \quad (27)$$

which agrees with the linear part of the latter integral Eq. (25). In Ref. 6, the analytic treatment is carried on by normalizing the time by $\gamma_L^* - \gamma_d$.

We observe that the relation (27) is a good approximation in most of the parameter space. However, as we get closer to the linear stability threshold, the relative error $|\gamma_L^* - \gamma_d - \gamma|/(|\gamma_L^* - \gamma_d| + |\gamma|)$ approaches unity. In addition, for our choice of distribution, there is a 14% discrepancy between the value of $\gamma_L^*/\omega_0 = 0.0373$ and $\gamma_L/\omega_0 = 0.0324$, the numerical solution of the eigenvalue problem. We infer that we can replace $\gamma_L^* - \gamma_d$ by γ in the integral Eq. (25) and use γ itself as the relevant choice of normalization parameter.

This procedure yields a steady solution,

$$\omega_b^2 = 2\sqrt{2}\nu_a^2\sqrt{\frac{\gamma}{\gamma_L^*}}. \quad (28)$$

A series of simulations near marginal stability ($0.005 < \gamma/\gamma_L < 0.02$), for ν_a spanning two orders of magnitude, confirms the validity of the latter expression. Figure 8 shows quantitative agreement with the saturation level of the numerical solutions.

Nonlinear stability analysis reveals that the constant solution (28) is unstable when $\nu_a < \nu_{\text{cr}}$, with $\nu_{\text{cr}} = 4.4\gamma$. To assess this criterion for the bifurcation from a steady-state solution to a periodic solution, a zoom in the behavior bifurcation diagram (Fig. 6) of the region near marginal stability where this bifurcation occurs is presented in Fig. 9. We observe a qualitative agreement between the steady-periodic boundary and ν_{cr}. However, when $\gamma/\gamma_L < 0.01$, chaotic solutions appear for $\nu \gg \nu_{\text{cr}}$. This discrepancy is explained by the existence of nonlinear excitations. As we approach marginal stability, the nonlinear behavior becomes sensible to the initial perturbation level. To prove this point, we perform a series of simulations in the vicinity of the bifurcation with an initial amplitude reduced from $\omega_b/\gamma_L = 0.3$ to $\omega_b/\gamma_L = 3 \times 10^{-7}$. Figure 10 shows the values of ν/γ for the bifur-
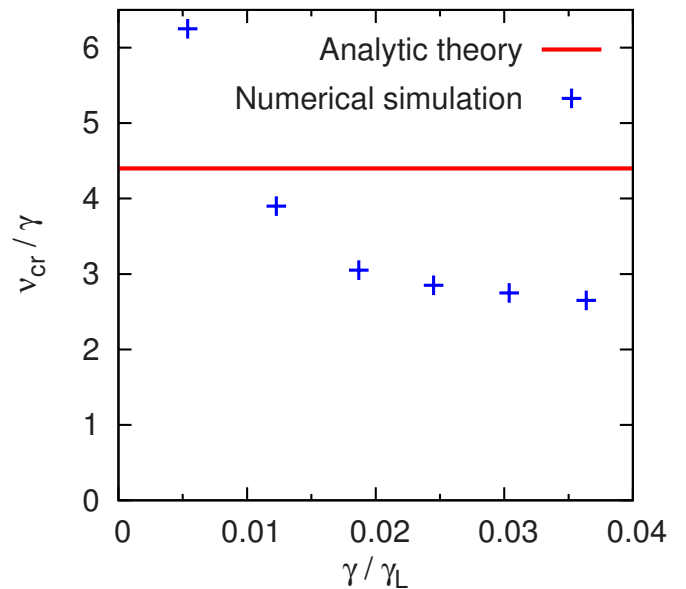

FIG. 10. (Color online) Critical distribution relaxation for steady state periodic bifurcation near marginal stability.
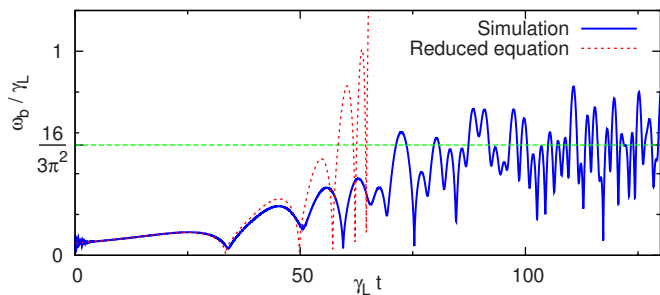
FIG. 11. (Color online) Time evolution of the normalized field amplitude, obtained from full-f simulation and from the reduced Eq. (25). In this simulation, the initial amplitude has been reduced to $\omega_b/\gamma_L=0.1$ to emphasize the behavior before saturation.

FIG. 12. (Color online) Logarithmic scale plot of the time evolution of the frequency power spectrum for $\gamma_d=0.938\gamma_L^*$, $\nu_a=2.7\times10^{-3}\gamma_L^*$. At each time, the spectrum is normalized to its maximum value.

cation between steady-state and periodic solutions. We confirm that ν_{cr}/γ stays close to the predicted value of 4.4 for smaller values of γ.

C. Frequency sweeping ($\nu_a < \gamma \leqslant \gamma_L$)

In the collisionless limit, the integral Eq. (25) is consistent with explosive solutions that diverge in a finite time, which suggests that the mode energy is partitioned into several spectral components. The resulting sideband frequencies have been observed to shift both upwardly and downwardly,[4] the frequency shift $\delta\omega(t)$ increasing in time, until the corresponding resonant velocities reach lower velocity gradient regions. Reference 8 shows how we can isolate one spectral component and model it by a BGK wave to obtain the time evolution of one chirping event. In the regime where $\ddot{\delta\omega}/\omega_b^3$, $\dot{\omega}_b/\omega_b^2$, and $\omega_b/\delta\omega \ll 1$, frequency sweeping is obtained as

$$\frac{\delta\omega(t)}{\gamma_L^*} = \frac{16}{3\pi^2}\sqrt{\frac{2}{3}\gamma_d t},\tag{29}$$

and a steady-state solution is given by

$$\omega_b/\gamma_L^* = 16/3\pi^2.\tag{30}$$

When γ_d is finite and ν_a is small enough, we observe such chirping solutions in our simulations. Figure 11 shows the time evolution of the field amplitude, when $\gamma_d=0.938\gamma_L^*$ and $\nu_a=2.7\times10^{-3}\gamma_L^*$, so that $\gamma=0.05\gamma_L^*$. The simulation result agrees with a numerical solution of the reduced Eq. (25), until the field amplitude exceeds the applicability limit. After saturation, the solution is close to the analytic prediction Eq. (30). Figure 12 shows the time evolution of the wave frequency power spectrum obtained with a moving Fourier window. Frequency sweeping events occur repetitively as the slope of the distribution is successively recovered and flattened. The time evolution of each chirping is slightly variable. To quantify the agreement with theory, we extract the 12 largest upshifting branches. In Fig. 13, we show these branches shifted to the same initial conditions, where each point is obtained by interpolating local maxima from the discrete frequency spectrum. From this plot, we conclude that before border effects occur, chirping evolution follows a square-root law in time, as expected from theory. This suggests a possibility to recover the product $\gamma_L^*\sqrt{\gamma_d}$ from such power spectrum. By fitting a square-root law to the branches
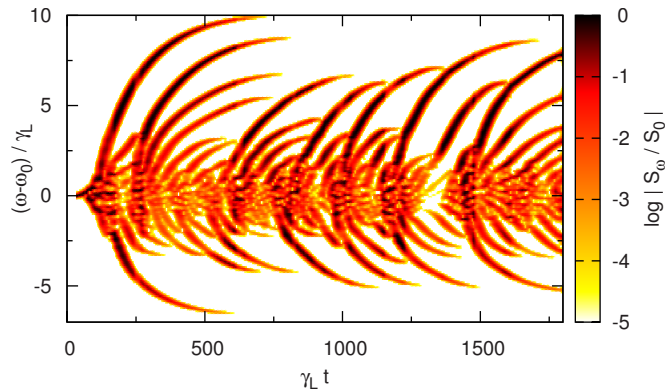
of Fig. 13, we obtain an average value of $\gamma_L^*\sqrt{\gamma_d}=0.0057$, with a standard deviation of 14%, when the input value is $\gamma_L^*\sqrt{\gamma_d}=0.0061$. When a plasma is close to marginal stability as in the experiment, we can assume $\gamma_L^*\sim\gamma_d$ ($\gamma_L^*\sqrt{\gamma_d}\sim\gamma_d^{3/2}$), and this chirping diagnostics may be used to estimate the extrinsic damping rate of the bulk plasma γ_d. The agreement of the expression Eq. (29) with chirping found in experimental devices[29] supports this claim. As we consider a single mode with a fixed wave number, a frequency sweeping corresponds to the evolution of some structures in the velocity distribution. In Fig. 14, we observe formation of hole and clump pairs in phase space, and they show clear correlation with peaks of the power spectrum shown in Fig. 12. It should be noted that near marginal stability, $\gamma_d>0.4\gamma_L$ is given as a necessary condition for hole-clump pair creation.[4] There is yet no theory in the opposite limit $\gamma\sim\gamma_L$, and in our simulations we observe frequency sweeping even when $\gamma_d\ll\gamma_L$.
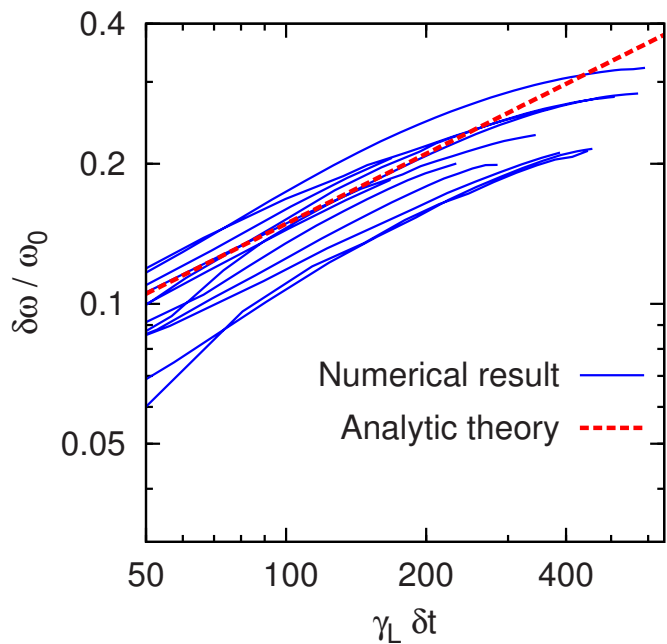

FIG. 13. (Color online) Time evolution of the 12 largest upshifting branches in logarithmic scale. The dashed curve is the analytic prediction Eq. (29).
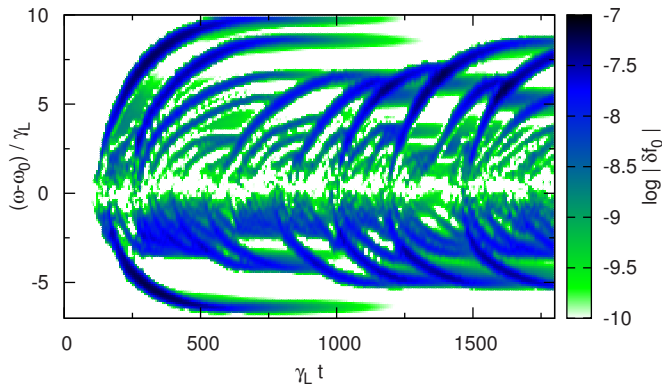
FIG. 14. (Color online) Logarithmic scale plot of the time evolution of $\delta f_0 \equiv \bar{f} - f_0$, normalized to n_0/v_{th}, for $\gamma_d = 0.938 \gamma_L^*$, $\nu_a = 2.7 \times 10^{-3} \gamma_L^*$.

The Fourier spectrum is shown in Fig. 15 for $\gamma_d / \gamma_L = 0.2$, $\nu_a / \gamma_L = 0.02$. Although the chirping is not as pronounced as in Fig. 12, we observe that the dominant frequency sweeps 5% of its initial value.

V. CONCLUSION

In this work, we presented a full-f Vlasov code to solve the BB model for a bump-on-tail distribution. The code was verified by checking its convergence and conservation properties, benchmarked against numerical simulations in former works, and validated against well-known linear and nonlinear theories.

We chose the plasma parameters so that we could explore the theory in several parameter regimes with the same initial distribution function. Since the theory considers the interaction between the wave and resonant particles only, we designed the collision operator so that collisions acted only on the beam particles. The feasibility of long-time simulations for a low-γ_L distribution hinged upon the quick convergence and strong stability properties of the CIP-CSL scheme. We performed a scan of the fully nonlinear evolution of the electric field in the whole (γ_d, ν_a) parameter space. A new diagnostics allowed us to identify the chirping region. Although holes and clumps were not expected to appear when $\gamma_d < 0.4 \gamma_L$, we found that the frequency sweeping region can expand to a low external dissipation regime, around $\gamma_d \approx 0.2 \gamma_L$. Also, nonlinearly unstable solutions in the linearly stable region have been detected. Numerical results show a good quantitative agreement with theory in several regimes.
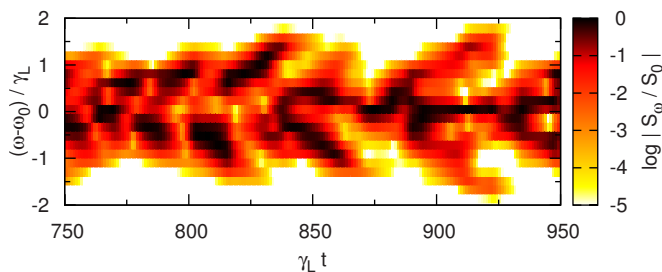

FIG. 15. (Color online) Logarithmic scale plot of the time evolution of the frequency power spectrum for $\gamma_d = 0.2 \gamma_L$, $\nu_a = 0.02 \gamma_L$.

The limits of validity correspond to the assumptions used in deriving the theory. A perturbative numerical approach which does not take into account the kinetic response of the bulk may feature spurious agreement outside of the validity limits when the resonant region reaches a non-negligible portion of bulk particles. We showed how one can identify γ_d by analyzing the time evolution of frequency shifting.

In future works, we will take a detailed look at the mechanism behind hole-clump pairs creation, and consider the dependency of chirping velocity to the time dependent slope of the distribution at the onset. We may also apply the theory of frequency sweeping to tokamak experiments. Moreover, subcritical instabilities will be investigated. It is important to understand the mechanism of such instabilities in the linearly stable region as an experimental device must take a path that go through this region as chirping emerges.

ACKNOWLEDGMENTS

APPENDIX A: THE CIP-CSL SCHEME

To solve the general 1D advection equation,

$$\partial_t F + u \partial_\lambda F = 0, \tag{A1}$$

in a conservative form, we evolve both F and its integrated value R. $\tilde{F}^n(\tilde{R}^n)$ is the continuous interpolated solution for $F(R)$ at the time $t_n = n\Delta t$. F_m^n is the discrete value of $\tilde{F}^n$ at the grid point of coordinate $\lambda_m = m\Delta\lambda$ and

$$R_m^n = \int_{\lambda_m}^{\lambda_{m+1}} \tilde{F}^n(\lambda) d\lambda. \tag{A2}$$

F^n is an array which contains the values F_m^n for every point m on a grid point of coordinate λ_m. We define the 1D algorithm CIPCSL1D $(u, F^n, F^{n+1}, R^n, R^{n+1}, \lambda, \Delta\lambda, \Delta t)$ as follows.

For each m,

- define $\lambda_{p_m} \equiv \lambda_m - u\Delta t$.
- Find the grid point k_m satisfying $\lambda_{k_m} \leq \lambda_{p_m} \leq \lambda_{k_m+1}$ and define $\langle \lambda_m \rangle \equiv \lambda_{p_m} - \lambda_{k_m}$.
- Define the coefficients

$$\phi_{k_m} \equiv \frac{F_{k_m}^n + F_{k_m+1}^n}{\Delta\lambda^2} - \frac{2R_{k_m}^n}{\Delta\lambda^3}, \tag{A3}$$

$$\eta_{k_m} \equiv -\frac{2F_{k_m}^n + F_{k_m+1}^n}{\Delta\lambda} + \frac{3R_{k_m}^n}{\Delta\lambda^2}. \tag{A4}$$

- Advect R,

$$R_m^{n+1} = R_{k_m}^n + D_{m+1}^n - D_m^n, \tag{A5}$$

where

$$D_m^n = \phi_{k_m}\langle\lambda_m\rangle^3 + \eta_{k_m}\langle\lambda_m\rangle^2 + F_m^n\langle\lambda_m\rangle. \tag{A6}$$

- Advect F,

$$F_m^{n+1} = 3\phi_{k_m}\langle\lambda_m\rangle^2 + 2\eta_{k_m}\langle\lambda_m\rangle + F_m^n. \tag{A7}$$

This 1D algorithm is extended to the 2D phase space (x,v) in the following way. $f_{i,j}^n$ is the value of the distribution f at the grid point of coordinates $x_i = i\Delta x$, $v_j = v_{\min} + j\Delta v$ at the time $t_n = n\Delta t$. We define the density within a cell and the line densities,

$$\rho_{i,j}^n = \int_{x_i}^{x_{i+1}}\int_{v_j}^{v_{j+1}} \widetilde{f}^n(x,v)\mathrm{d}x\mathrm{d}v, \tag{A8}$$

$$\sigma_{xi,j}^n = \int_{x_i}^{x_{i+1}} \widetilde{f}^n(x,v_j)\mathrm{d}x, \tag{A9}$$

$$\sigma_{vi,j}^n = \int_{v_j}^{v_{j+1}} \widetilde{f}^n(x_i,v)\mathrm{d}v. \tag{A10}$$

The first advection in the x-direction is performed by calling successively, for each j,

CIPCSL1D$(\bar{v}_j, \sigma_v^n, \sigma_v^*, \rho^n, \rho^*, x, \Delta x, \Delta t/2)$,

CIPCSL1D$(v_j, f^n, f^*, \sigma_x^n, \sigma_x^*, x, \Delta x, \Delta t/2)$,

with $\bar{v}_j \equiv (v_j + v_{j+1})/2$. Similarly, the advection in the v-direction is performed by calling successively, for each i,

CIPCSL1D$(q\bar{E}_i/m, \sigma_x^*, \sigma_x^{**}, \rho^*, \rho^{**}, v, \Delta v, \Delta t)$,

CIPCSL1D$(qE_i/m, f^*, f^{**}, \sigma_v^*, \sigma_v^{**}, v, \Delta v, \Delta t)$,

with $\bar{E}_i \equiv (E_i + E_{i+1})/2$. Then we repeat the advection in the x-direction,

CIPCSL1D$(\bar{v}_j, \sigma_v^{**}, \sigma_v^{n+1}, \rho^{**}, \rho^{n+1}, x, \Delta x, \Delta t/2)$,

CIPCSL1D$(v_j, f^{**}, f^{n+1}, \sigma_x^{**}, \sigma_x^{n+1}, x, \Delta x, \Delta t/2)$.

Here, the subscripts $*$ and $**$ were used to designate intermediate steps between t_n and t_{n+1}. To avoid spurious leakage of particles, we impose a zero flux at the velocity boundaries by setting

$$\langle\lambda_{j=1}\rangle = \langle\lambda_{j=N_v}\rangle = 0. \tag{A11}$$

APPENDIX B: TIME-SERIES CATEGORIZATION ALGORITHM

The algorithm we developed to categorize the behavior of each numerical solution is an improved version of the algorithm designed by Vann,[7] with an other way of sorting out chaotic from periodic behavior, a new diagnostics to distinguish chirping from merely chaotic solutions, and where we take into account numerical issues, which appear when γ_L is smaller.

The categorization is based on an analysis of the time series of the normalized electric field energy, $A(t) \equiv \mathcal{E}(t)/\mathcal{E}_0$, with $\mathcal{E}_0 = n_0 m v_{\mathrm{th}}^2/2$. First, we define the global minimum as $A_{\mathrm{gm}} \equiv \min\{A(t)\}_{0<t<t_{\max}}$, where $t_{\max}$ is the time duration of the simulation. Then we drop the initial transient phase and extract a time window $t_{\min} < t < t_{\max}$ over which $A(t)$ is sampled at a rate Δt_s. Here, $t_{\min}$ is an estimation of the time duration of the transient phase. Within this window, we define the mean value $\langle A\rangle$, maximum $A_{\max} \equiv \max\{A(t)\}$ and minimum $A_{\min} \equiv \min\{A(t)\}$, the oscillation amplitude $\Delta A \equiv A_{\max} - A_{\min}$, and the local minima (maxima) as points where $A(t)$ is smaller (larger) than $A(t-\Delta t_s)$ and $A(t+\Delta t_s)$. As a measure of the periodicity, we compute the two point correlation function as

$$R(\tau) = \frac{1}{m}\sum_{j=0}^{m-1} \frac{\langle\widetilde{A}_j(\tau,\tau')\widetilde{A}_{j+1}(\tau,\tau')\rangle}{\sqrt{\langle\widetilde{A}_j(\tau,\tau')^2\rangle}\sqrt{\langle\widetilde{A}_{j+1}(\tau,\tau')^2\rangle}}, \tag{B1}$$

where for each correlation window size τ,

$$\widetilde{A}_j(\tau,\tau') \equiv A(t_{\max} - j\tau - \tau') - \langle A(t_{\max} - j\tau)\rangle. \tag{B2}$$

$m = (t_{\max} - t_{\min})/\tau$ is the number of period included inside the total time window and the angular brackets represent the time-average over a period,

$$\langle\widetilde{A}(\tau,\tau')\rangle = \frac{1}{\tau}\int_0^\tau \widetilde{A}(\tau,\tau')\mathrm{d}\tau'. \tag{B3}$$

The overall correlation R_0 is defined as the maximum of $R(\tau)$ for $\tau > \tau_c$, where τ_c is the shortest period such that $R(\tau_c) \leq 0$. In other words, R_0 is the normalized amplitude of the peak in the two point correlation function corresponding to the dominant frequency. This measure which is used to sort out chaotic from periodic behavior is different from the one given in Ref. 7. We also provide a criterion to sort out chirping solutions. We compute the frequency power spectrum of the time evolution of the electric field at some position, $E(x=0,t)$, and normalize the amplitude of the spectrum to its maximum value. At each time, we extract the largest and smallest frequency for which the amplitude in the power spectrum is significant, i.e., larger than a threshold ϵ_6. Then, we define $\Delta\omega_{\max}$ as the maximum difference between the largest and smallest frequency, normalized to the plasma frequency. We then proceed to the following decision tree:

(1) if $A_{\mathrm{gm}} < \epsilon_0$, then damped.
(2) Else if $\Delta\omega_{\max} > \epsilon_7$, then chirping.
(3) Else if $\langle A\rangle < \epsilon_1$, then damped.
(4) Else if $A(t)$ is monotonic and $\Delta A/\langle A\rangle < \epsilon_2$, then steady-state.
(5) Else if $A(t)$ is monotonically decreasing (zero local extrema), then damped.
(6) Else if each minima (maxima) is larger (smaller) than the former or $\Delta A/\langle A\rangle < \epsilon_3$ or $\Delta A < \epsilon_4$, then steady-state.
(7) Else if $R_0 > 1 - \epsilon_5$, then periodic.
(8) Else if the number of extrema is not less than four then chaotic,

where ϵ_i are thresholds that must be carefully adjusted. Spe-

cial care is taken in adjusting ϵ_7 empirically so that frequency splitting is not mistaken for frequency sweeping.

In this decision tree, the logical test B3 is an addition to the one given in Ref. 7. For damped solutions, as the electric field becomes small, the particles experience free streaming, leading to spurious recurrence effects after half the recurrence time $T_R/2 = \pi/k\Delta v$. Free streaming occurs when $|qE_0|T_R/m < \Delta v$, and ϵ_0 is chosen to reflect this condition. For the benchmark, this logical step is switched off as the recurrence effect is less problematic for shorter-time simulations.

[1] H. V. Wong and H. L. Berk, Phys. Plasmas **5**, 2781 (1998).

[2] X. Garbet, G. Dif-Pradalier, C. Nguyen, P. Angelino, Y. Sarazin, V. Grandgirard, P. Ghendrih, and A. Samain, AIP Conf. Proc. **1069**, 271 (2008).

[3] H. L. Berk, B. N. Breizman, and M. S. Pekker, Plasma Phys. Rep. **23**, 778 (1997).

[4] B. N. Breizman, H. L. Berk, M. S. Pekker, F. Porcelli, G. V. Stupakov, and K. L. Wong, Phys. Plasmas **4**, 1559 (1997).

[5] A. Fasoli, B. N. Breizman, D. Borba, R. F. Heeter, M. S. Pekker, and S. E. Sharapov, Phys. Rev. Lett. **81**, 5564 (1998).

[6] H. L. Berk, B. N. Breizman, and M. Pekker, Phys. Rev. Lett. **76**, 1256 (1996).

[7] R. G. L. Vann, R. O. Dendy, G. Rowlands, T. D. Arber, and N. d'Ambrumenil, Phys. Plasmas **10**, 623 (2003).

[8] H. L. Berk, B. N. Breizman, and N. V. Petviashvili, Phys. Lett. A **234**, 213 (1997).

[9] H. L. Berk, B. N. Breizman, and N. V. Petviashvili, Phys. Lett. A **238**, 408 (1998).

[10] H. L. Berk, B. N. Breizman, J. Candy, M. Pekker, and N. V. Petviashvili, Phys. Plasmas **6**, 3102 (1999).

[11] H. L. Berk and B. N. Breizman, Phys. Fluids B **2**, 2246 (1990).

[12] T. Nakamura, R. Tanaka, T. Yabe, and K. Takizawa, J. Comput. Phys. **174**, 171 (2001).

[13] I. B. Bernstein, J. M. Greene, and M. D. Kruskal, Phys. Rev. **108**, 546 (1957).

[14] B. Breizman, H. Berk, and H. Ye, Phys. Fluids B **5**, 3217 (1993).

[15] P. Bhatnagar, E. Gross, and M. Krook, Phys. Rev. **94**, 511 (1954).

[16] M. Lesur, Y. Idomura, and S. Tokuda, JAEA-Research **2006–089**, 1, 2007.

[17] T. Nakamura and T. Yabe, Comput. Phys. Commun. **120**, 122 (1999).

[18] C. Cheng and G. Knorr, J. Comput. Phys. **22**, 330 (1976).

[19] G. Strang, SIAM (Soc. Ind. Appl. Math.) J. Numer. Anal. **5**, 506 (1968).

[20] H. L. Berk, B. N. Breizman, and M. Pekker, Phys. Plasmas **2**, 3007 (1995).

[21] J. R. Cary and I. Doxas, J. Comput. Phys. **107**, 98 (1993).

[22] L. Landau, J. Phys. (Paris) **10**, 25 (1946).

[23] B. Davies, J. Comput. Phys. **66**, 36 (1986).

[24] B. D. Fried, C. S. Liu, R. W. Means, and R. Z. Sagdeev, National Technical Information Service Document No. AD730123 PGG-93, University of California, Los Angeles (1971). Copies may be ordered from the National Technical Information Service, Springfield, Virginia 22161.

[25] E. Fijalkow, Comput. Phys. Commun. **116**, 319 (1999).

[26] F. Xiao, T. Yabe, G. Nizam, and T. Ito, Comput. Phys. Commun. **94**, 103 (1996).

[27] F. Xiao, T. Yabe, X. Peng, and H. Kobayashi, J. Geophys. Res., [Atmos.] **107**, 4609, doi:10.1029/2001JD001532 (2002).

[28] H. L. Berk, B. N. Breizman, and H. Ye, Phys. Rev. Lett. **68**, 3563 (1992).

[29] S. D. Pinches, H. L. Berk, D. N. Borba, B. N. Breizman, S. Briguglio, A. Fasoli, G. Fogaccia, M. P. Gryaznevich, V. Kiptily, M. J. Mantsinen et al., Plasma Phys. Controlled Fusion **46**, B187 (2004).